

The liquid flow in multi-stage flash evaporators

OSAMU MIYATAKE and TOSHIYUKI HASHIMOTO

Department of Chemical Engineering, Kyushu University, Fukuoka 812, Japan

and

NOAM LIOR

Department of Mechanical Engineering and Applied Mechanics, University of Pennsylvania, Philadelphia, PA 19104-6315, U.S.A.

(Received 30 August 1991 and in final form 21 February 1992)

Abstract—In an attempt to reach a quantitative understanding of the interaction between the fluid mechanics and flash evaporation in a stage of a multi-stage flash (MSF) evaporator, and in horizontal free-surface streams in general, a numerical analysis is performed, as a first step, of two-dimensional turbulent isothermal flow of a liquid in a flash chamber (stage) with and without a baffle (sill) placed downstream of the inlet orifice. Experiments are also performed, and validate the model successfully in the range of flows of 4.3×10^5 – 8.7×10^5 kg h⁻¹ (m width)⁻¹ and liquid level of 0.4 m, conditions typical to MSF evaporators. The baffle plate is found to serve well in propelling the entering liquid to the free surface and in generating low-pressure regions, primarily near the stream line rising from the top edge of the baffle, both effects promoting evaporation rates. The interstage orifice coefficient is found to be practically independent of the liquid superheat, temperature, and mass flow rate.

1. INTRODUCTION

ALTHOUGH multi-stage flash (MSF) evaporators are widely used in water desalination, producing most of the desalted water in the world today, the complexity of the flow, heat transfer and vapor release phenomena in these devices still hinders detailed modeling and innovative improvements of the process. Even the empirical correlations developed for characterizing the vapor release rate and the approach to thermodynamic equilibrium in tested designs provide results which may differ by up to about one order of magnitude from each other [1].

Well-documented in the engineering literature (cf. refs. [2–4]), the process in its simplest form is shown in Fig. 1. The liquid being distilled (e.g. brine or seawater) flows through a number of successive stages, with the vapor pressure decreasing from stage to stage in the direction of the liquid flow. The liquid flows through an inlet aperture into a region where the pressure is lower than its saturation pressure, and flashing is therefore initiated. The emanating vapor is condensed on a tube bundle which also serves as a distilland preheater, and drips into distillate collection trays. A demister is placed in the vapor path to reduce carryover of distilland droplets into the distillate trays. As the liquid evaporates it also cools down along its path in a stage and thus approaches the thermodynamic equilibrium dictated by its temperature and concentration and by the vapor pressure and temperature in the stage. The vapor is released from the

liquid by both bubble formation (this primarily in the hydraulic jump near the exit from the interstage aperture) and by free-surface evaporation (cf. ref. [5]). Since the evaporation rate is thus typically higher near the free surface, a negative temperature gradient develops in the liquid in the upward direction. The vapor release rate and the approach to thermodynamic equilibrium, parameters most critical in the evaporator performance, are directly linked to the heat transfer in the stage, which most strongly depends on the fluid dynamics there.

Studies of such flash evaporators were so far primarily experimental (cf. refs. [5–9]), in order to both understand the process physics and set the stage necessary for the theoretical modeling of these complicated flow and heat and mass transfer phenomena. In this study the isothermal flow in such a flash chamber (stage) is modeled mathematically. This provides information for the hydrodynamic design of such chambers and constitutes the first necessary step for the theoretical modeling of heat and mass transfer in flash evaporation from free-surface horizontal streams. Furthermore, even without experimental justification, it is reasonable to predict that flow patterns existing in the isothermal case would be at least applicable for the cases in which the superheat is small and flash evaporation occurs near the free surface. Previous experimental observations by the authors [5, 8] have shown that generally the difference in flow patterns between the isothermal and non-isothermal cases is not too large because the flow pattern is domi-

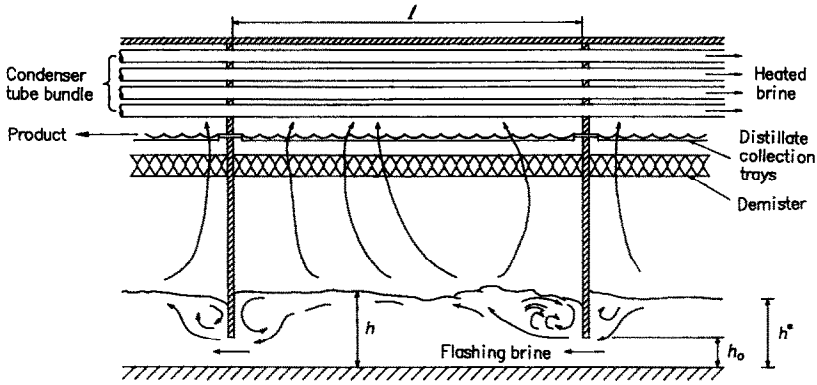


FIG. 1. A typical stage in a multi-stage flash evaporator.

Beyond direct applicability to MSF evaporators, the study provides fundamental insights into the behavior of free-surface horizontal streams which flow through apertures.

2. MATHEMATICAL FORMULATION

2.1. The governing equations

Consider a steady, two-dimensional turbulent flow of liquid in a flash chamber (stage) with a vertical baffle plate (sill) as shown in Fig. 2. Since in practical applications such flash chambers are typically wider than 10 m, three-dimensional effects may be ignored. Flow visualization in our experiments described below has shown that this is a reasonable assumption even in narrower chambers. The solution domain is the interior of the liquid region under the free surface as depicted in Fig. 2.

Since the temperature variation in a stage is small, of the order of a few degrees Celsius at most, constant liquid properties can be assumed. The governing equations, momentum and mass conservation, expressed as the vorticity (ω) transport equation using the stream function (ψ), are for an isothermal flow

$$\frac{\partial}{\partial x} \left(\omega \frac{\partial \psi}{\partial y} \right) - \frac{\partial}{\partial y} \left(\omega \frac{\partial \psi}{\partial x} \right) = \nu \left(\frac{\partial^2 \omega}{\partial x^2} + \frac{\partial^2 \omega}{\partial y^2} \right) + I_t \quad (1)$$

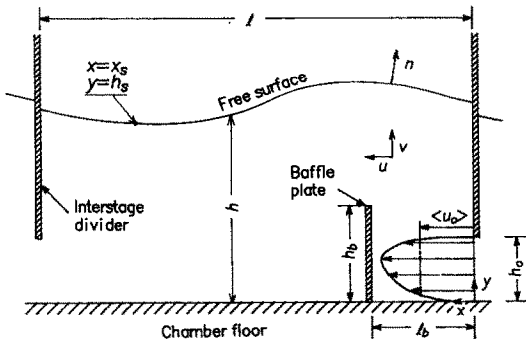


FIG. 2. Model description in a flash chamber (stage).

$$\omega = - \left(\frac{\partial^2 \psi}{\partial x^2} + \frac{\partial^2 \psi}{\partial y^2} \right) \quad (2)$$

where

$$I_t = - \left(\frac{\partial^2}{\partial x^2} - \frac{\partial^2}{\partial y^2} \right) (\rho \overline{u'v'}) + \frac{\partial^2}{\partial x \partial y} [\rho (\overline{u'^2} - \overline{v'^2})] \quad (3)$$

$$u = \frac{\partial \psi}{\partial y} \quad (4)$$

and

$$v = - \frac{\partial \psi}{\partial x}. \quad (5)$$

Using the definition of the turbulent eddy viscosity, μ_t , the first term of the right-hand side of equation (3) may be expressed as

$$\begin{aligned} - \left(\frac{\partial^2}{\partial x^2} - \frac{\partial^2}{\partial y^2} \right) (\rho \overline{u'v'}) &= \left(\frac{\partial^2}{\partial x^2} - \frac{\partial^2}{\partial y^2} \right) \\ &\times \left[\mu_t \left(\frac{\partial u}{\partial y} + \frac{\partial v}{\partial x} \right) \right] = \left(\frac{\partial^2}{\partial x^2} + \frac{\partial^2}{\partial y^2} \right) (\mu_t \omega) \\ &+ 2 \left[\frac{\partial^2}{\partial x^2} \left(\mu_t \frac{\partial u}{\partial y} \right) - \frac{\partial^2}{\partial y^2} \left(\mu_t \frac{\partial v}{\partial x} \right) \right]. \quad (6) \end{aligned}$$

In the flow regions near the walls (interstage divider, baffle plate, and chamber floor) and near the free surface of the liquid, the second terms of the right hand sides of equations (3) and (6) are small compared with the respective first terms. Since the flow pattern in a flash chamber is dominated by the flows in these regions, I_t may be reduced to

$$I_t \approx \left(\frac{\partial^2}{\partial x^2} + \frac{\partial^2}{\partial y^2} \right) (\mu_t \omega). \quad (7)$$

The eddy viscosity is expressed by the generalized Prandtl mixing-length hypothesis (cf. ref. [10])

$$\mu_t = \rho l_m^2 \left[\left(\frac{\partial u}{\partial y} \right)^2 + \left(\frac{\partial v}{\partial x} \right)^2 \right]^{1/2}. \quad (8)$$

These equations are non-dimensionalized by defining the following non-dimensional variables

$$\begin{aligned}\Psi &= \frac{\psi}{\langle u_o \rangle h_o}, \quad \Omega = \frac{\omega h_o}{\langle u_o \rangle}, \quad U = \frac{u}{\langle u_o \rangle}, \quad V = \frac{v}{\langle u_o \rangle} \\ Re &= \frac{\langle u_o \rangle h_o}{\nu}, \quad M = \frac{\mu_t}{\mu}, \quad L_m = \frac{l_m}{h_o} \\ X &= \frac{x}{h_o}, \quad Y = \frac{y}{h_o}, \quad N = \frac{n}{h_o}, \quad L = \frac{l}{h_o} \\ L_b &= \frac{l_b}{h_o}, \quad H = \frac{h}{h_o}, \quad H_b = \frac{h_b}{h_o}.\end{aligned}\quad (9)$$

The resulting dimensionless equations are

$$\begin{aligned}\frac{\partial}{\partial X} \left(\Omega \frac{\partial \Psi}{\partial Y} \right) - \frac{\partial}{\partial Y} \left(\Omega \frac{\partial \Psi}{\partial X} \right) \\ = \frac{1}{Re} \left(\frac{\partial^2}{\partial X^2} + \frac{\partial^2}{\partial Y^2} \right) [(1+M)\Omega]\end{aligned}\quad (10)$$

$$\Omega = - \left(\frac{\partial^2 \Psi}{\partial X^2} + \frac{\partial^2 \Psi}{\partial Y^2} \right)\quad (11)$$

where

$$M = Re L_m^2 \left[\left(\frac{\partial U}{\partial Y} \right)^2 + \left(\frac{\partial V}{\partial X} \right)^2 \right]^{1/2}\quad (12)$$

$$U = \frac{\partial \Psi}{\partial Y}\quad (13)$$

and

$$V = - \frac{\partial \Psi}{\partial X}.\quad (14)$$

Assuming zero shear stress at the free surface and no slip at the walls, the following dimensionless boundary conditions are obtained:

$$X = 0 \quad \text{or} \quad L, \quad 1 \leq Y \leq H; \quad \Psi = 1, \quad \partial \Psi / \partial X = 0\quad (15)$$

$$0 \leq X \leq L, \quad Y = 0; \quad \Psi = \partial \Psi / \partial Y = 0\quad (16)$$

$$0 < X < L, \quad Y = H; \quad \Psi = 1, \quad \partial^2 \Psi / \partial N^2 = 0\quad (17)$$

$$X = L_b, \quad 0 < Y \leq H_b; \quad \Psi = \partial \Psi / \partial X = 0\quad (18)$$

$$0 < Y < 1; \quad (\Psi)_{X=0} = (\Psi)_{X=L}, \quad (\Omega)_{X=0} = (\Omega)_{X=L}.\quad (19)$$

Equation (19) means that the velocity distributions at the inlet orifice and the outlet orifice are identical (a reasonable assumption in such MSF evaporators because the mass flow rate of liquid and the orifice opening do not change much from stage to stage). Thus, after each iterative calculations of Ψ and Ω for the whole solution domain, the values of $(\Psi)_{X=0}$ and $(\Omega)_{X=0}$ are replaced with the calculated values of $(\Psi)_{X=L}$ and $(\Omega)_{X=L}$, respectively.

2.2. Mixing-length distribution

The following dimensionless scales are introduced for characterizing the mixing-length:

$$S = \frac{s}{h_o}, \quad \Delta = \frac{\delta}{h_o}\quad (20)$$

in which s is the inward normal distance from the horizontal or vertical walls, and δ is the characteristic width of turbulent flow. The mixing-lengths near the wall are taken as 0.41 times the distance to the nearest wall, and those in the core of the solution domain are taken as 0.09 times the characteristic width of turbulent flow, that is

$$\begin{aligned}L_m &= 0.41S \quad (S/\Delta \leq 0.09/0.41) \\ L_m &= 0.09\Delta \quad (S/\Delta > 0.09/0.41).\end{aligned}\quad (21)$$

This formula is valid for boundary layers near a single wall and velocity distributions with maxima (e.g. wall jets) when δ is taken as the boundary layer thickness, and also for plane jets in stagnant surroundings with δ taken as the half-width of the jet [11]. As shown qualitatively in Fig. 3(a), the flow field is composed of a number of distinctly different flow regimes which also possess different characteristic scales. In an attempt to determine the minimal number of scales (flow regimes) needed for accurate computation of the flow, computations were made for one and two regions in the case of the stage without a baffle ('Empty') as shown in Fig. 3(b), and for one, three, and four regions in the more complex case where a baffle is placed in the stage ('Baffle') as shown in Fig. 3(c). Corresponding to the description in Figs. 3(b) and (c), the division of the solution domain into the various regions with different mixing length distributions, and the Δ chosen for each model were as follows.

Without a baffle plate (Empty)

$$\left. \begin{aligned}(\text{a) Model E1} \\ \Delta = H. \\ (\text{b) Model E2} \\ \text{Region (I-E2)}; \Delta = H_1 \\ \text{Region (II-E2)}; \Delta = H_2/2.\end{aligned} \right\} \quad (22)$$

With a baffle plate (Baffle)

$$\left. \begin{aligned}(\text{a) Model B1} \\ \Delta = H. \\ (\text{b) model B2} \\ \text{Region (I-B2)}; \Delta = 1 \quad (L_b \geq 1), \\ \Delta = L_b \quad (L_b < 1) \\ \text{Region (II-B2)}; \Delta = H_1/2 \\ \text{Region (III-B2)}; \Delta = H_2. \\ (\text{c) Model B3} \\ \text{Region (I-B3)}; \Delta = 1/2 \quad (L_b \geq 1), \\ \Delta = L_b/2 \quad (L_b < 1) \\ \text{Region (II-B3)}; \Delta = H_1/2 \\ \text{Region (III-B3)}; \Delta = H_2 \\ \text{Region (IV-B3)}; \Delta = H_3.\end{aligned} \right\} \quad (23)$$

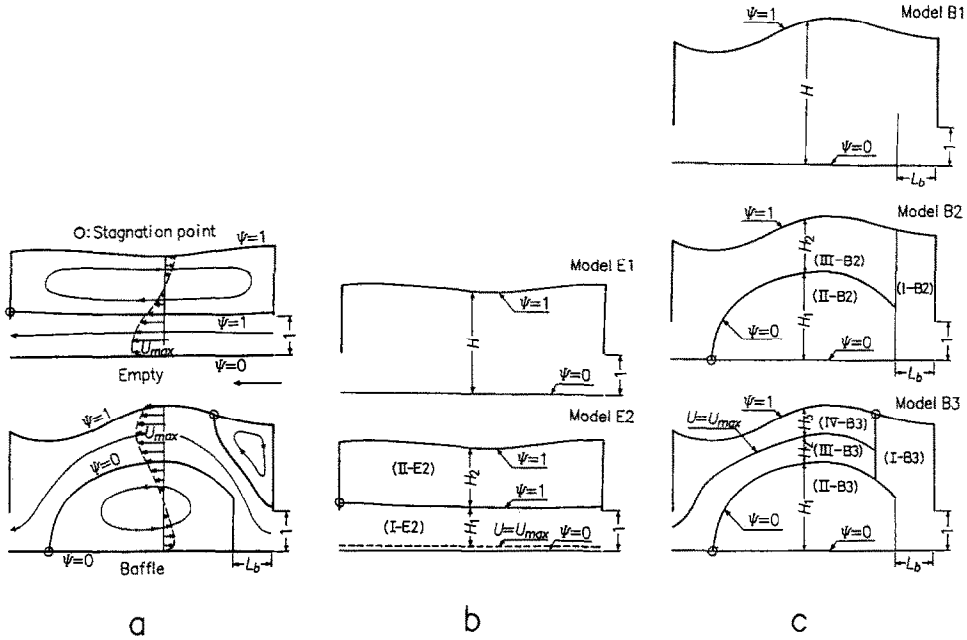


FIG. 3. Turbulent flow regimes used in the model. (a) Typical flow patterns in: stage without a baffle ('Empty'); stage with a baffle ('Baffle'). (b) Stage without a baffle ('Empty'): single flow regime (Model E1); two flow regimes (Model E2). (c) Stage with a baffle ('Baffle'): single flow regime (Model B1); three flow regimes (Model B2); four flow regimes (Model B3).

2.3. Pressure distribution

Given the pressure at the free surface, the pressure distribution in the liquid can be computed from the y -component of the momentum equation

$$u \frac{\partial v}{\partial x} + v \frac{\partial v}{\partial y} = -\frac{1}{\rho} \frac{\partial p}{\partial y} + \nu \left(\frac{\partial^2 v}{\partial x^2} + \frac{\partial^2 v}{\partial y^2} \right) - \frac{\partial \overline{u'v'}}{\partial x} - \frac{\partial \overline{v'^2}}{\partial y} - g. \quad (24)$$

Denoting the absolute values of the third and fourth term on the right-hand side of equation (24) as $\alpha = |\partial \overline{u'v'} / \partial x|$ and $\beta = |\partial \overline{v'^2} / \partial y|$, then $\alpha \ll \beta$ if $u \gg v$ [12]. Based on Ornstein's experimental results [7], $\beta < 0.6 \text{ m s}^{-2}$ for the range of parameters in this study, small compared with the gravitational acceleration, g . Consequently both terms α and β can be neglected in the chamber regions in which the horizontal flow is predominant. However, when the vertical baffle is present in the chamber, $v > u$ in the region upstream of the baffle and there $\alpha \gg \beta$, where α may have the order of g . Only the fourth term (β) on the right-hand side of equation (24) was therefore neglected here. The dimensionless form of the thus-reduced equation (24) is

$$\frac{\partial P}{\partial Y} = - \left(U \frac{\partial V}{\partial X} + V \frac{\partial V}{\partial Y} \right) + \frac{1}{Re} \left\{ \left(\frac{\partial^2 V}{\partial X^2} + \frac{\partial^2 V}{\partial Y^2} \right) + \frac{\partial}{\partial X} \left[M \left(\frac{\partial U}{\partial Y} + \frac{\partial V}{\partial X} \right) \right] \right\} - \frac{1}{Fr} \quad (25)$$

where

$$P = \frac{p}{\rho \langle u_o \rangle^2} \quad \text{and} \quad Fr = \frac{\langle u_o \rangle^2}{gh_o}. \quad (26)$$

2.4. The interstage orifice coefficient

The interstage orifice (aperture) coefficient, C , is an important parameter in the hydrodynamic design of flash chambers. C is defined by the equation

$$C = \langle u_o \rangle \left[\frac{1 - (h_o/h^*)^2}{2g(\Delta h + \Delta p/\rho g)} \right]^{1/2} \quad (27)$$

or in dimensionless form

$$C = \left[\frac{1 - (1/H^*)^2}{2(\Delta H/Fr + \Delta P)} \right]^{1/2} \quad (28)$$

where

$$H^* = \frac{h^*}{h_o}, \quad \Delta H = \frac{\Delta h}{h_o} \quad \text{and} \quad \Delta P = \frac{\Delta p}{\rho \langle u_o \rangle^2}. \quad (29)$$

Typically the liquid level in all stages of the MSF evaporator is the same and the flow is driven by the interstage vapor pressure differences, so $H^* = H$ and $\Delta H/Fr \ll \Delta P$, reducing equation (28) to

$$C = \left[\frac{1 - (1/H)^2}{2\Delta P} \right]^{1/2}. \quad (30)$$

The pressure drop ΔP can be calculated in this case from the viscous dissipation rate of mechanical energy per unit mass flow rate of liquid in the flash chamber, which is (cf. ref. [13])

$$\phi = \frac{(\xi)_{x=0} - (\xi)_{x=L}}{\langle u_o \rangle h_o} \quad (31)$$

where

$$\xi = \int_0^h \left(\frac{u^2 + v^2}{2} + \frac{p}{\rho} + gy \right) u \, dy. \quad (32)$$

The functions ϕ and ξ become in dimensionless form

$$\Phi = (\Xi)_{X=0} - (\Xi)_{X=L} \quad (33)$$

and

$$\Xi = \int_0^H \left(\frac{U^2 + V^2}{2} + P + \frac{Y}{Fr} \right) U \, dY \quad (34)$$

where

$$\Phi = \frac{\phi}{\langle u_o \rangle^2} \quad \text{and} \quad \Xi = \frac{\xi}{\langle u_o \rangle^3 h_o}. \quad (35)$$

Since here $\Delta P = \Phi$, equation (30) becomes

$$C = \left[\frac{1 - (1/H)^2}{2\Phi} \right]^{1/2}. \quad (36)$$

3. THE EXPERIMENTAL APPARATUS AND PROCEDURE

In a flash chamber without a baffle plate (empty stage) and with a baffle plate, in the range of fresh water flow rates of $W = 4.3 \times 10^5 - 8.7 \times 10^5 \text{ kg h}^{-1}$ (m width) $^{-1}$ and a water level of 0.40 m at $x = 0.775$ m (values typical to MSF evaporators), the following experiments were carried out: (1) measurement of flow patterns and pressure distributions in the liquid, using fresh water maintained at 60°C (without flashing); (2) determination of the effects of the Reynolds number and the flash chamber geometry on the flow pattern, and measurement of the orifice coefficient, C , using flashing fresh water in the temperature range of 40–80°C.

The experimental apparatus, shown in Figs. 4 and 5, is a three-stage flash evaporator, the second stage being the test stage, with each stage consisting of a flash chamber and a condenser. The three flash chambers, each 1.0 m long and 0.046 m wide, are separated from each other by vertical plate dividers, and a rectangular orifice, 0.15 m high and 0.046 m wide, for the transport of liquid is located at the bottom of each divider. Ample windows are available for flow observation.

Air is evacuated from the system prior and during the evaporation experiments. Separate loops are used for the condenser cooling water and for the flash evaporator. The temperature of the water in each of these two loops can be regulated independently, as shown in Fig. 4. Before admission to the lowest temperature stage condenser, the condenser coolant can be cooled by means of a chiller to a level necessary for condensation of the vapor produced in that stage. Heat is added to the flash evaporator water in an external

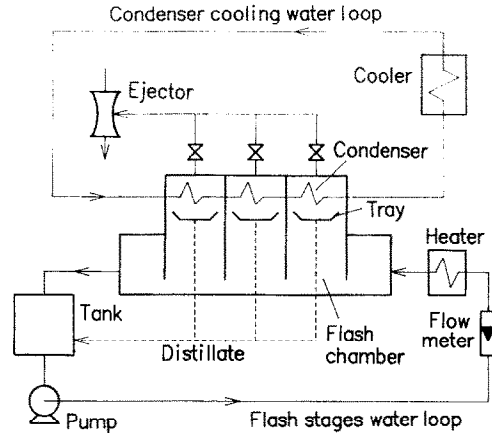


FIG. 4. Flow diagram of the experimental apparatus.

heater to bring its inlet temperature to the desired level. Next the hot water is admitted to the highest temperature stage where it flashes, and continues to flash in the second (test) stage and the third stage, because of exposure to decreasing vapor pressures chambers.

Temperature measurements were made with copper-constantan sheathed thermocouples, 1 mm diameter. They were calibrated in reference to a standard thermometer, and the measurement accuracy was $\pm 0.05^\circ\text{C}$.

The flow rate of the water was measured by a rotameter which was calibrated to an accuracy of $\pm 3\%$ through the full range of water temperatures used in the experiment.

The local water velocity measurements in the stage were made by analyzing photographs taken for a precisely-known exposure time of the motion of water-saturated round paper chips, all ~ 1.5 mm dia., added to the water. The slip velocity was negligible. To improve measurement accuracy despite velocity fluctuations, the streaks of five chips at each measurement location were examined in each photograph. From the measurement of the streak length and knowledge of the exposure time for each frame, the average velocity for each point was thus calculated. Considering the errors in the exposure time, optical error of the frame-analysis projector, and the visual reading error, it is estimated that the accuracy of the velocity measurement was within $\pm 4\%$.

The pressure distribution was measured by photographically recording the level of water in 13 vertical sight glasses, connected to the water via 1 mm diameter taps placed along a vertical line in the chamber wall, located at $x = 0.28$ m. The measurement accuracy was estimated to be ± 0.2 mm water column.

4. THE NUMERICAL ANALYSIS

4.1. Shape of the free surface

The free surface contour $y = h(x)$ or $Y = H(X)$ which passes through the arbitrary standard point



FIG. 5. The three-stage flash evaporator.

$y = h_s$ at $x = x_s$ or $Y = H_s$ at $X = X_s$ (see Fig. 2) was approximated in this study by the polynomial equation

$$H - H_s = f(W) \sum_{n=2}^4 K_n (X^n - X_s^n) \quad (37)$$

in which $f(W)$ is a function of liquid flow rate W , and K_n ($n = 2-4$) is a constant, both determined experimentally.

It was found from the experiments carried out for $h_0 = 0.15$ m and $h_s = 0.40$ m at $x_s = 0.775$ m ($H_s = 0.40/0.15$ at $X_s = 0.775/0.15$) that $f(W)$ is given by the expression

$$f(W) = [W/(6.52)10^5]^2 \quad (38)$$

and that the coefficients K_n ($n = 2-4$) have the values shown in Table 1.

4.2. The numerical method

Starting with an assumed Ψ field which satisfies the boundary conditions described by equations (15)–(19), the elliptic partial differential equation (10) is solved to obtain new values of Ω by using the upwind method. The values of U and V needed in the term M (equation (12)) are obtained from the values of Ψ by

using equations (13) and (14) and central-differencing. Also using a central-difference approximation for the second derivatives of Ψ , and from the values of Ω , equation (11) with the same boundary conditions (15)–(19) is then solved to obtain new values of Ψ . Values of Ω at the boundaries are obtained by developing and using a third order polynomial relationship of $\Psi(X)$ and $\Psi(Y)$. The changes in the values of H_1 , H_2 , and H_3 , which define the regions with the different turbulence scales, are also computed successively, with consequent adjustments of the turbulent scales to satisfy equations (21)–(23). If the differences between the new and previous values of Ψ are not within 10^{-4} at all nodal points, the new values of Ψ are substituted and the procedure is repeated until this criterion is satisfied.

The computations were repeated for grid sizes of 41×41 , 81×81 , and 161×161 , and typical results of the influence of grid size are shown in Fig. 6. Within this range of grid sizes, the results were significantly dependent on grid size only in the region of the orifice and baffle, near the stage entrance. Results which are grid-size-independent for practical purposes, were obtained for a grid of 81×81 , used in all the subsequent computations shown in this paper.

Table 1. Coefficients of the free surface shape correlation, equation (37)

l_b [m]	h_b [m]	K_2	$K_3 \times 10$	$K_4 \times 10^2$
—	0	-0.079	0.266	-0.224
0.15	0.20	0.210	-0.858	0.807
0.22	0.20	0.189	-0.761	0.710
0.28	0.20	0.167	-0.664	0.613
0.15	0.15	0.186	-0.707	0.650
0.15	0.10	0.161	-0.556	0.492

($l = 1.00$ m, $h_0 = 0.15$ m) ($X_s = 0.775/0.15$, $H_s = 0.40/0.15$). $W = 4.3 \times 10^3 \sim 8.7 \times 10^5$ kg h⁻¹ m⁻¹.

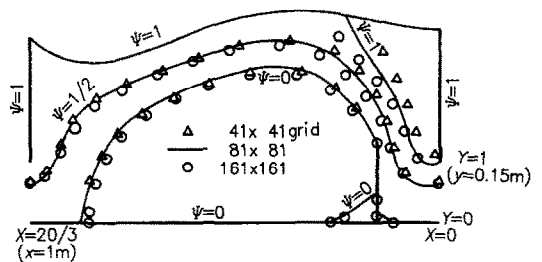


FIG. 6. The effect of grid size on the computed streamlines. Stage with a baffle ('Baffle'), $Re = 3.9 \times 10^3$, $l_b = 0.15$ m, $h_b = 0.20$ m.

The pressure distributions were computed from equation (25). The velocity gradients in this equation were computed by spline interpolation of the numerical results for U , V , and M . The boundary condition was the given constant pressure at the free surface.

4.3. Computation of the interstage orifice coefficient

The interstage orifice coefficient, C , described in Section 2.4 above, was calculated from equation (36), where Φ was obtained from equations (33) and (34) by Simpson's-rule integration of the velocity and pressure distribution data computed from the theoretical model described in Sections 2.1–2.3 above.

4.4. The range of the numerical analysis

Corresponding with the flash chamber geometry of the experimental apparatus, computations have been made for $l = 1.0$ m, $h_0 = 0.15$ m, $l_b = 0.15$ – 0.28 m, $h_b = 0$ – 0.20 m (Fig. 2) and $h = h_0 = 0.40$ m at $x = x_s = 0.775$ m, for water flow rates of 4.3×10^5 – 8.7×10^5 kg h⁻¹ (m width)⁻¹, as shown in Table 1.

5. RESULTS

5.1. Turbulent mixing length scaling

Figure 7 shows a comparison of typical computed and measured horizontal velocity distributions at $x = 0.28$ m, using the different turbulent mixing length scaling regions described in Section 2.2 above. The experimental results were obtained by measuring the motion of the paper chips, as described in Section 3.

Although the measured values exhibit some scatter due to the fluctuations of the liquid flow, the computations with the two-region model (E2) for the empty stage, and the four-region model (B3) for the stage with the baffle gave results which were closest to the experimental data (within about 5%), showing good agreement between the theory and the experiments. Models E2 and B3 were thus used in the computations which generated the results shown in this paper.

5.2. The flow rate parameter

While the mass flow rate of saline water through a typical MSF evaporator diminishes by only up to about 10% due to evaporation, and therefore the mass flow rate in each stage is almost constant, the Reynolds number has a more drastic variation due to the change in the water temperature. For example, as the temperature changes from 80 to 40°C, the Reynolds number for a constant flow rate $W = 6.5 \times 10^5$ drops from 5.1×10^5 to 2.8×10^5 in this experimental apparatus. The effect of the Reynolds number on the flow pattern at constant mass flow rate was investigated, and the results are shown in Fig. 8. It was found that the 82% variation in Reynolds number, corresponding to temperature variation from 40 to 80°C, had negligible effect on the streamlines (and consequently velocity) profiles for a constant mass flow rate.

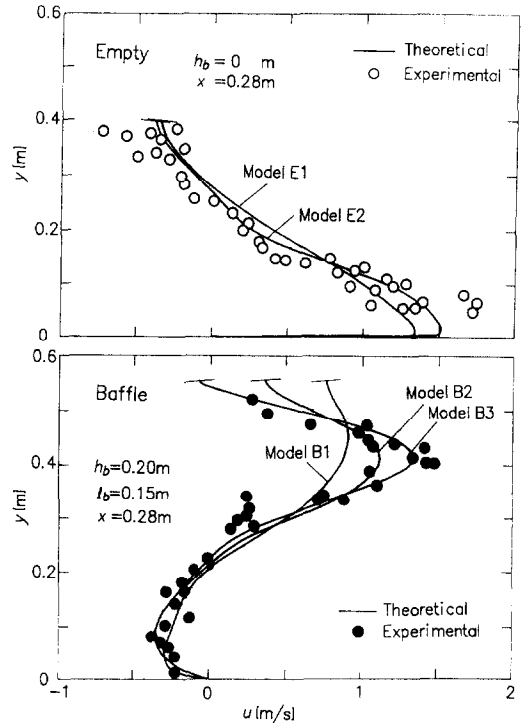


FIG. 7. Comparison of the computed and experimental velocity profiles using different turbulent flow regime models. Top: stage without a baffle ('Empty'). Bottom: stage with a baffle ('Baffle'). $Re = 3.9 \times 10^5$.

The numerical results below are shown by taking the mass flow rate, W , evaluated from the Reynolds number at 60°C, as the mass flow parameter.

5.3. Flow patterns

The computed contour maps of the stream function in a 1.0 m long flash chamber without a baffle plate and with a baffle plate are shown in Figs. 9 and 10. The stream enters the chamber from the right. Without a baffle plate, the entering liquid flows near the bottom of the chamber (with the main forward-flow at a depth approximately equal to the vertical opening of the interstage orifice) and runs through to the next stage, with a recirculating flow (which overlays the forward-flow) taking place near the free surface. In the case of

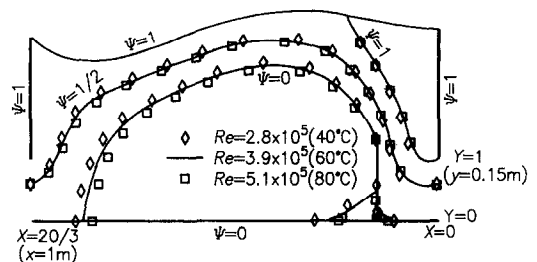


FIG. 8. Effect of the Reynolds number on the streamlines. Stage with a baffle ('Baffle'), $W = 6.5 \times 10^5$ kg h⁻¹ m⁻¹, $l_b = 0.15$ m, $h_b = 0.20$ m.

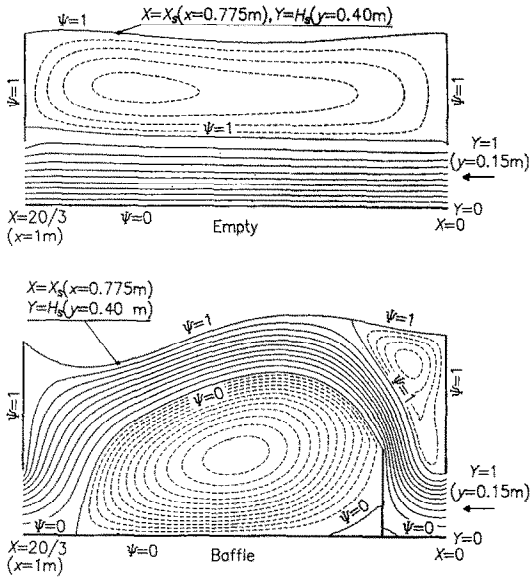


FIG. 9. Detailed streamline maps. Top: stage without a baffle ('Empty'). Bottom: stage with a baffle ('Baffle'). $W = 6.5 \times 10^5 \text{ kg h}^{-1} \text{ m}^{-1}$, $l_b = 0.15 \text{ m}$, $h_b = 0.20 \text{ m}$. The spacing, $\Delta\psi$, between neighboring solid streamlines is 0.1, and that between neighboring broken streamlines is 0.04.

a short flash chamber, say 1.0 m long, the submerged jet of liquid emanating from the inlet orifice does not meet the free surface due to the influence of the downstream inter-stage divider. Consequently, there is no flow region where the velocity distribution tends to become vertically uniform above the chamber floor, as observed in a comparatively long flash chamber such as shown by Gilbert [6] for a chamber 3.45 m long.

On the other hand, when a baffle plate is installed in the chamber, it causes the liquid entering the flash chamber to be projected upwards and to flow near the free surface with two main recirculating flows taking place: one near the bottom of the chamber and the other above the inlet orifice. In an evaporating stream the baffle thus serves to improve the exposure of entering superheated liquid to the lower pressure regions near the free surface. Within the range of parameters in this study, higher baffles placed closer to the inter-stage orifice improve this exposure, but also increase the interstage pressure loss. This indicates that an optimal baffle height and location exists.

The corresponding theoretically- and experimentally-obtained streamlines for isothermal flows are compared by their superposition in Fig. 11. The streamlines were visualized in the experiments by observing the movement of water-saturated paper chips added into the water. The agreement between theory and experiments is seen to be excellent.

5.4. Static pressure distribution

To facilitate quantitative understanding of the evaporation phenomena in such stages, the computed static pressure distributions for each flow pattern shown in Fig. 10 are shown in Figs. 12 and 13 in the form of saturation temperature isotherm maps, corresponding to the static pressure. Figure 12 shows a full detail of the saturation isotherms in one experimental case. The densely spaced isotherms in the entrance and downstream floor regions were omitted from the reduced-size contours presented in Figure 13, for better visual clarity. The contour lines with

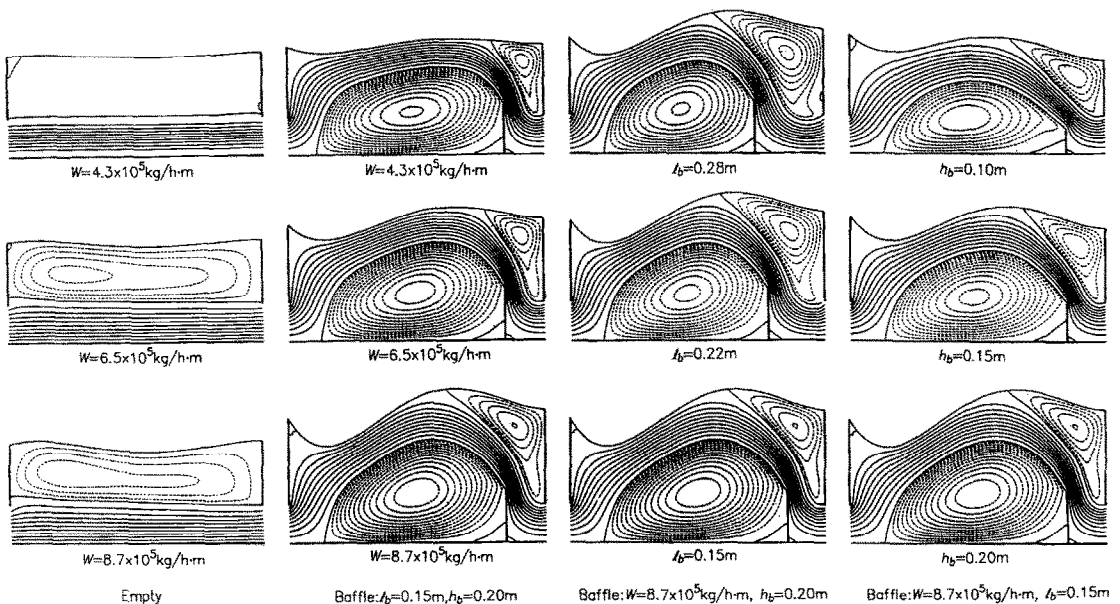


FIG. 10. Streamline maps for different flow rates and configurations. The spacing, $\Delta\psi$, between neighboring solid streamlines is 0.1, and that between neighboring broken streamlines is 0.04. The legends and other clarifications are the same as shown in Fig. 9.

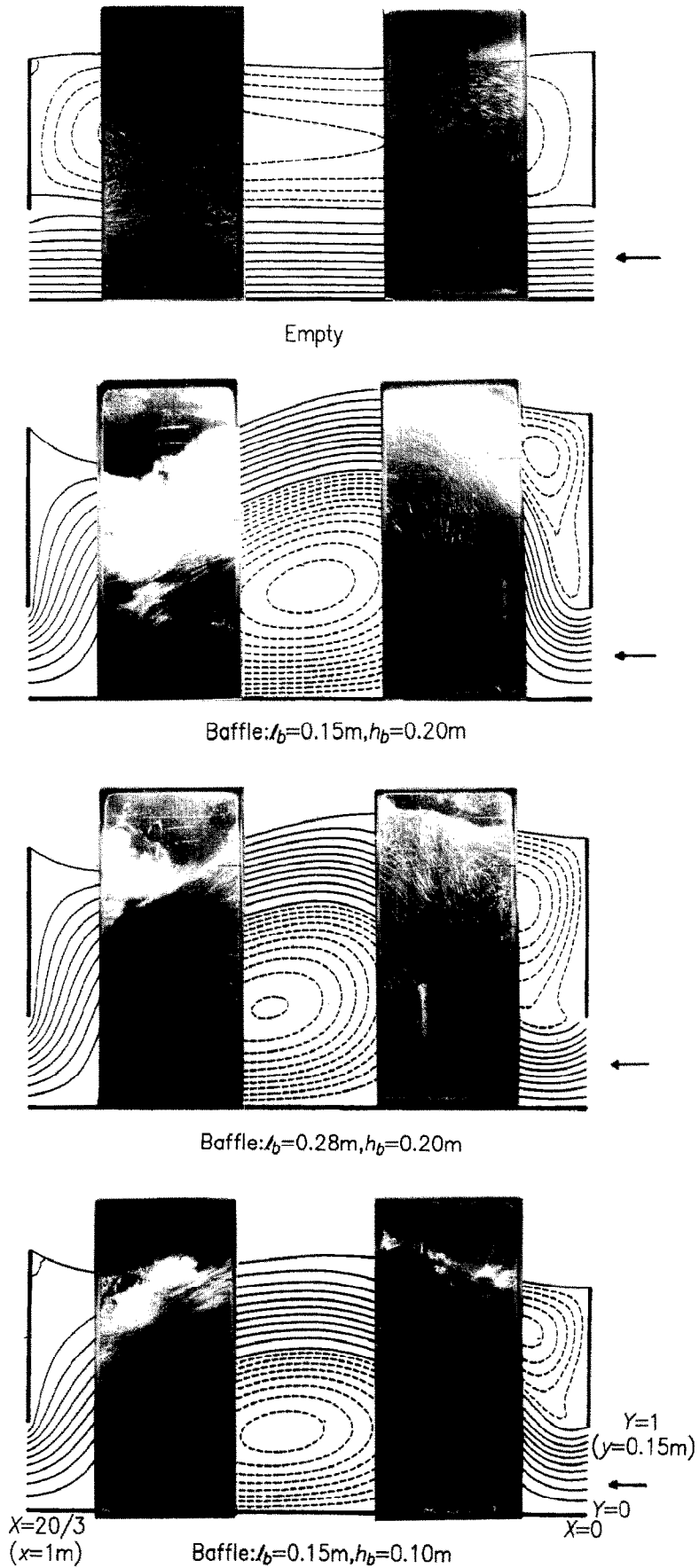


FIG. 11. Comparison of computed and experimental flow patterns. $W = 6.5 \times 10^3 \text{ kg h}^{-1} \text{ m}^{-1}$.

Table 2. The conditions for the isobar (saturation isotherm) maps shown in Figs. 12 and 13

	$(T_s)_{fs}$		
	40°C	60°C	80°C
①	$T_s = 40.00^\circ\text{C}$ $p_s = 7.375 \times 10^3 \text{ Pa}$	$T_s = 60.00 \text{ C}$ $p_s = 19.920 \times 10^3 \text{ Pa}$	$T_s = 80.00^\circ\text{C}$ $p_s = 47.360 \times 10^3 \text{ Pa}$
②	$T_s = 42.27^\circ\text{C}$ $p_s = 8.316 \times 10^3 \text{ Pa}$	$T_s = 61.00 \text{ C}$ $p_s = 20.861 \times 10^3 \text{ Pa}$	$T_s = 80.48^\circ\text{C}$ $p_s = 48.301 \times 10^3 \text{ Pa}$
③	$T_s = 44.40^\circ\text{C}$ $p_s = 9.293 \times 10^3 \text{ Pa}$	$T_s = 62.00 \text{ C}$ $p_s = 21.838 \times 10^3 \text{ Pa}$	$T_s = 80.98^\circ\text{C}$ $p_s = 49.278 \times 10^3 \text{ Pa}$
④	$T_s = 46.43^\circ\text{C}$ $p_s = 10.310 \times 10^3 \text{ Pa}$	$T_s = 63.00 \text{ C}$ $p_s = 22.855 \times 10^3 \text{ Pa}$	$T_s = 81.49^\circ\text{C}$ $p_s = 50.295 \times 10^3 \text{ Pa}$
⑤	$T_s = 48.36^\circ\text{C}$ $p_s = 11.367 \times 10^3 \text{ Pa}$	$T_s = 64.00 \text{ C}$ $p_s = 23.912 \times 10^3 \text{ Pa}$	$T_s = 82.01^\circ\text{C}$ $p_s = 51.352 \times 10^3 \text{ Pa}$
⑥	$T_s = 50.21^\circ\text{C}$ $p_s = 12.464 \times 10^3 \text{ Pa}$	$T_s = 65.00 \text{ C}$ $p_s = 25.009 \times 10^3 \text{ Pa}$	$T_s = 82.54^\circ\text{C}$ $p_s = 52.449 \times 10^3 \text{ Pa}$
⑦	$T_s = 51.99^\circ\text{C}$ $p_s = 13.605 \times 10^3 \text{ Pa}$	$T_s = 66.00 \text{ C}$ $p_s = 26.150 \times 10^3 \text{ Pa}$	$T_s = 83.08^\circ\text{C}$ $p_s = 53.590 \times 10^3 \text{ Pa}$
⑧	$T_s = 53.70^\circ\text{C}$ $p_s = 14.789 \times 10^3 \text{ Pa}$	$T_s = 67.00 \text{ C}$ $p_s = 27.334 \times 10^3 \text{ Pa}$	$T_s = 83.64^\circ\text{C}$ $p_s = 54.774 \times 10^3 \text{ Pa}$

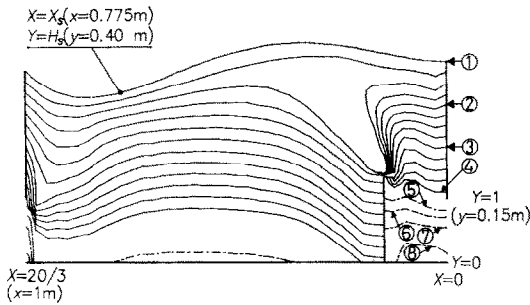


FIG. 12. Detailed isobar (or saturation isotherm) maps. Stage with a baffle ('Baffle'). $W = 6.5 \times 10^5 \text{ kg h}^{-1} \text{ m}^{-1}$, $l_b = 0.15 \text{ m}$, $h_b = 0.20 \text{ m}$. For the conditions see Table 2. The separation between dash-dotted contours is four times that between the solid contours.

encircled numbers correspond to the saturation temperatures, T_s , (for saturation pressure P_s) shown in Table 2 for the saturation temperatures at the free surface, $(T_s)_{fs}$, of 40, 60 and 80°C.

As seen from Figs. 12 and 13, a low pressure region appears along the streamline emitted from the top of the baffle plate, and the amount of that pressure reduction increases with the flow rate W .

Figure 14 presents comparisons of the theoretical pressure distribution in the vertical direction in the liquid region at $x = 0.28 \text{ m}$ with experimental measurements which were obtained by reading the height of the liquid in 13 vertical sight glasses (cf. Section 3 above).

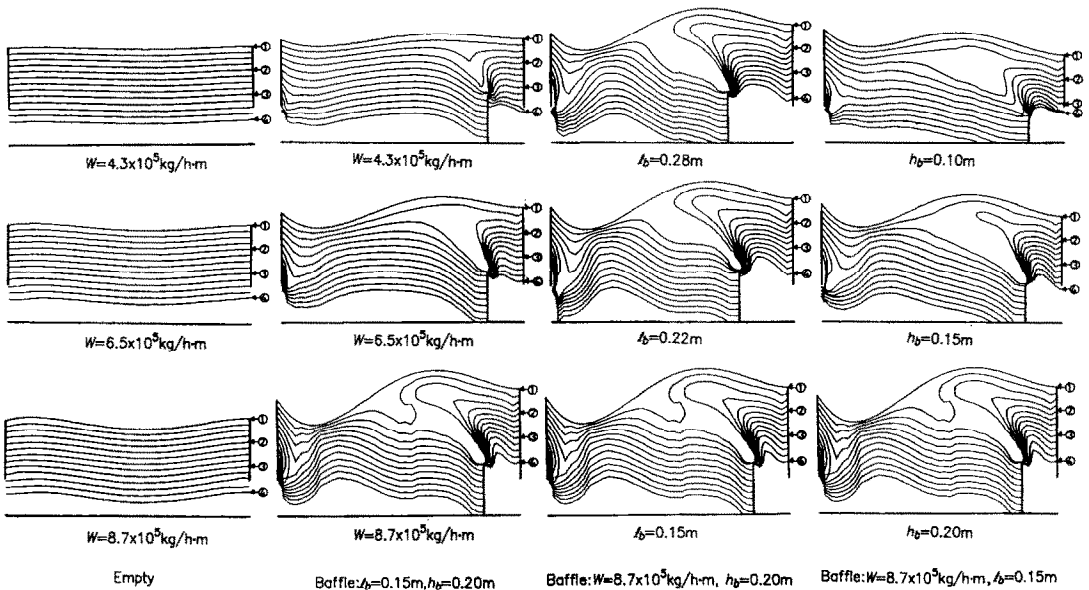


FIG. 13. Isobar (or saturation isotherm) maps for different flow rates and configurations. For the conditions see Table 2. The legends and other clarifications are the same as shown in Fig. 12.

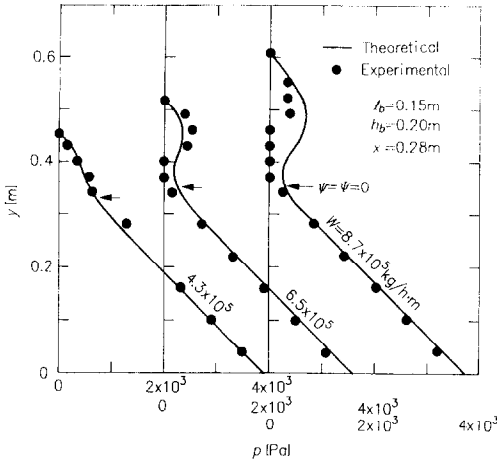


FIG. 14. Comparison of numerical and experimental pressure distributions. Stage with a baffle ('Baffle').

It is clear from Fig. 14 that the pressure decreases near the location where the streamline emanating from the top of the baffle plate ($\psi = \Psi = 0$) passes, followed by a linear increase with increasing depth. The lower pressure regions are the likely sites for bubble growth and consequently for higher vapor release rates in a flash evaporation stage of this design.

The agreement between theory and experiments is good for small flow rates (W), but less satisfactory for the highest flow rate of $W = 8.7 \times 10^5 \text{ kg h}^{-1} \text{ (m width)}^{-1}$, due to a breakup in the liquid stream which occurred along the streamline coming from the top of the baffle plate, in the low pressure region depicted in Figs. 12 and 13, at this high flow rate.

5.5. The interstage orifice coefficient

The interstage orifice coefficient, C , for isothermal flow in the chamber was evaluated from the numerical solutions of the velocity and pressure distributions, as described in Section 2.4 above.

Figure 15 shows the comparisons of the theoretical results for isothermal flow ($\Delta T_s = 0$) and the experimental results for flow with flashing ($\Delta T_s > 0$), where $\Delta T_s = T_i - T_v$ is defined here as the liquid superheat. It appears from the experimental results that the orifice coefficient is practically independent of superheat, ΔT_s , or temperature, indicating that isothermal flow modeling in such flash chambers, and within the range of parameters considered in this study, provides hydrodynamic results which are also valid in the case of flows with flashing, as long as the flashdown temperature difference is relatively small.

As can be expected, C decreases as baffle height h_b increases and as the distance l_b from the baffle to the orifice decreases. C also slightly increases with flow rate.

6. CONCLUSIONS

- A numerical model was developed for describing the isothermal turbulent fluid dynamics of free-surface flow in a stage of a typical multi-stage flash (MSF) evaporator with and without a baffle plate (sill) downstream of the interstage orifice. The model was validated successfully by experiments up to the flow rate at which the stream breaks up.

- It was possible to obtain a remarkably good prediction of this complex turbulent flow field by the use of a conventional mixing-length model. This was achieved by a break-down of the flow field into a number of regions in which different, though conventional, scaling was used for the mixing length.

- The shape of the free surface in this model was provided from an empirical correlation developed in this study for that purpose. It was found that the flow pattern for a constant mass flow rate of liquid per unit chamber width, W , is not affected by changes in the Reynolds number due to the temperature dependency

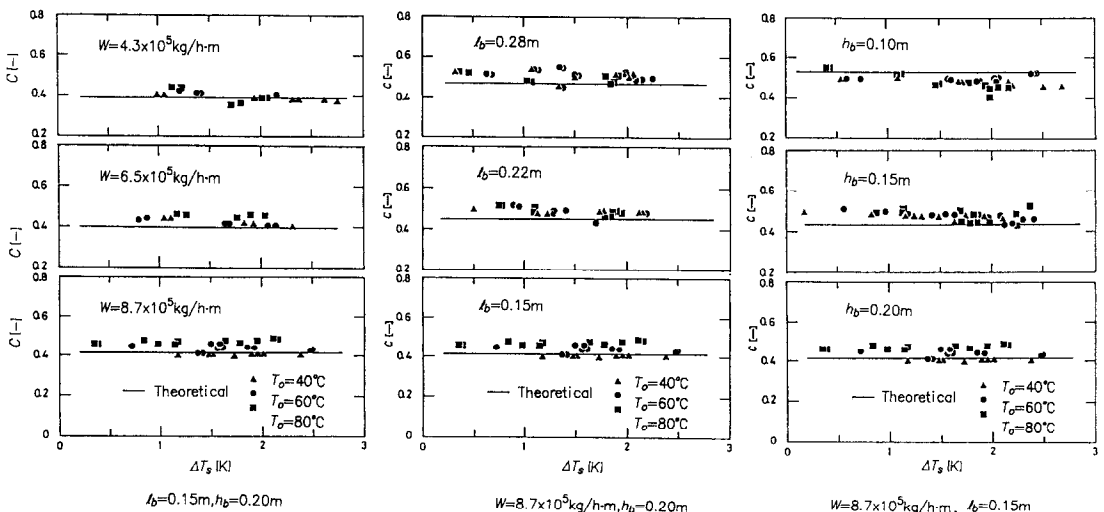


FIG. 15. Comparison of computed and experimental orifice coefficients. Stage with a baffle ('Baffle'), for different flow rates and configurations.

of the thermophysical properties in the range of 40–80°C, leaving W as the dominant flow parameter.

- The baffle plate (sill) serves well to propel the entering liquid to the free surface and to generate low-pressure regions, primarily near the stream line rising from the top edge of the baffle, both effects promoting evaporation rates. The size of this low-pressure region and the degree of pressure reduction increase with flow rate and baffle height, and are practically independent of the baffle distance from the orifice.

- The interstage orifice coefficient, C , is practically independent of the superheat ΔT_s and of the liquid temperature. It decreases as the height of the baffle increases and as the baffle-to-orifice distance decreases. Although it also increases slightly with the mass flow rate, this change is negligible.

REFERENCES

1. N. Lior, Formulas for calculating the approach to equilibrium in open-channel flash evaporators, *Desalination* **60**, 223–249 (1986).
2. Burns and Roe, Inc., Universal design: report on design of a 2.5 Million gallon per day universal desalting plant, United States Department of the Interior Contract No. 14-01-0001-955 (available from the Superintendent of Documents, U.S. Government Printing Office, Washington, DC 20402) (June 1969).
3. A. Porteous, *Saline Water Desalination Processes*. Longman, London (1975).
4. A. H. Khan, *Desalination Processes and Multi-stage Flash Distillation Practice*. Elsevier, Amsterdam (1986).
5. N. Lior and R. Greif, Some basic observations on heat transfer and evaporation in the horizontal flash evaporator, *Desalination* **33**, 269–286 (1980).
6. F. W. Gilbert, An experimental investigation of steady state characteristics of flashing salt solutions in open channel flow between two submerged orifices at low pressure. Ph.D. Thesis, University of Connecticut, Storrs, Connecticut (1968).
7. H. L. Ornstein, An investigation of turbulent open channel flow simulating water desalination flash evaporators. Ph.D. Thesis, University of Connecticut, Storrs, Connecticut (1970).
8. O. Miyatake, T. Fujii and T. Hashimoto, An experimental study of multi-stage flash evaporation phenomena, *Heat Transfer—Jpn Res.* **6**, 25–35 (1977).
9. N. Lior and R. Greif, A system for the experimental study of flash evaporation, *Desalination* **31**, 87–89 (1979).
10. A. D. Gosman, W. M. Pun, A. K. Runchal, D. B. Spalding and M. Wolfshtein, *Heat and Mass Transfer in Recirculating Flows*, p. 186. Academic Press, London (1969).
11. B. E. Launder and D. B. Spalding, *Mathematical Models of Turbulence*, pp. 27, 29. Academic Press, London (1972).
12. J. O. Hinze, *Turbulence*, p. 378. McGraw-Hill, New York (1959).
13. R. B. Bird, W. E. Stewart and E. N. Lightfoot, *Transport Phenomena*, p. 211. Wiley, New York (1976).